Modeling of Polar Ocean Tides at the Last Glacial Maximum: Amplification, Sensitivity, and Climatological Implications

STEPHEN D. GRIFFITHS AND W. RICHARD PELTIER

Department of Physics, University of Toronto, Toronto, Ontario, Canada

(Manuscript received 19 March 2008, in final form 24 November 2008)

ABSTRACT

Diurnal and semidiurnal ocean tides are calculated for both the present day and the Last Glacial Maximum. A numerical model with complete global coverage and enhanced resolution at high latitudes is used including the physics of self-attraction and loading and internal tide drag. Modeled present-day tidal amplitudes are overestimated at the standard resolution, but the error decreases as the resolution increases. It is argued that such results, which can be improved in the future using higher-resolution simulations, are preferable to those obtained by artificial enhancement of dissipative processes. For simulations at the Last Glacial Maximum a new version of the ICE-5G topographic reconstruction is used along with density stratification determined from coupled atmosphere–ocean climate simulations. The model predicts a significant amplification of tides around the Arctic and Antarctic coastlines, and these changes are interpreted in terms of Kelvin wave dynamics with the aid of an exact analytical solution for propagation around a polar continent or basin. These polar tides are shown to be highly sensitive to the assumed location of the grounding lines of coastal ice sheets, and the way in which this may contribute to an interaction between tides and climate change is discussed. Globally, the picture is one of energized semidiurnal tides at the Last Glacial Maximum, with an increase in tidal dissipation from present-day values, the dominant energy sink being the conversion to internal waves.

1. Introduction

Tides occur throughout the oceans as periodic oscillations in currents and sea surface height, typically with diurnal or semidiurnal time scales. The amplitude of the surface oscillations is about 50 cm over much of the open ocean and about 1 m along many coastlines, but local resonances can lead to tides of over 5 m in special coastal locations (e.g., Garrett 1972; Arbic et al. 2007). However, tidal amplitudes are sensitive to the frequency of the lunar and solar forcing (i.e., the length of the day), the ocean depth and density stratification, and the coastal configuration. Considerable changes in each of these over the history of the earth must have led to corresponding changes in ocean tides. For instance, modeling studies of the Last Glacial Maximum (LGM) have shown that the implied sea level drop of about 120 m leads to considerable amplification of semidiurnal tides (Thomas and Sündermann 1999; Egbert et al. 2004; Arbic et al. 2004b; Uehara et al. 2006; Griffiths and Peltier 2008; Arbic et al. 2008). Such changes can impact the climate system in a variety of ways.

Globally, of interest is the history of tidal dissipation, which is mainly associated with energy loss to a turbulent bottom boundary layer in shallow seas (Taylor 1920) and conversion to internal tides in the deep ocean (e.g., Garrett and Kunze 2007). Tidal dissipation implies a slowing of the earth's rotation rate and a corresponding recession of the moon, variations in which can be traced back over two billion years (Williams 2000). Furthermore, the portion of energy converted to internal tides is thought to play an important role in vertical mixing of the deep ocean (e.g., Wunsch 2000). Changes to this mixing rate could lead to changes in ocean circulation and climate, as discussed by Wunsch (2005), Munk and Bills (2007), and Montenegro et al. (2007). Tidal models, in which dissipation is parameterized, suggest that both internal tide dissipation and total dissipation were considerably higher at LGM than at present (Egbert et al. 2004; Uehara et al. 2006).

Corresponding author address: Dr. Stephen D. Griffiths, Department of Applied Mathematics, University of Leeds, Leeds LS2 9JT, United Kingdom.
E-mail: sdg@maths.leeds.ac.uk

DOI: 10.1175/2008JCLI2540.1

On a smaller scale, past variations in tidal amplitudes may have local significance. At high latitudes, recent attention has been focused on amplification of semidiurnal tides under glacial conditions in the Labrador Sea (Arbic et al. 2004b, 2008) and the Arctic Ocean (Griffiths and Peltier 2008), and how these large tides might have interacted with adjoining ice streams and shelves to cause rapid climate change events. On the northwest European shelf, postglacial changes in tidal amplitudes, currents, and mixing were examined by Uehara et al. (2006). They, and others (e.g., Shennan and Horton 2002), have shown that changes in tidal amplitudes over the Holocene need to be accounted for when interpreting sedimentary records used to construct relative sea level history. We note that a corresponding analysis of changes in tidal range is needed for the east coast of North America, where there is disagreement between predictions and observations of relative sea level in the interval 5000–10 000 yr before present (Peltier 1998, his Fig. 23).

Here we present new simulations of global tides at LGM. At this time, ice sheets covered much of northern Europe and Canada, and the changes to the ocean depth and coastal configuration were the most extreme over recent history. Using a range of datasets and numerical models, several studies have suggested that there were also significant changes to the tides. Although the likely pattern of the semidiurnal tides at LGM has now been established, the studies of Egbert et al. (2004) and Arbic et al. (2004b, 2008) did not resolve the Arctic Ocean (for numerical reasons), that of Uehara et al. (2006) did not include a full treatment of tidal self-attraction and loading, while that of Thomas and Sündermann (1999) was performed at a low resolution, which required the use of nonphysical damping. We avoid all of these shortfalls by using the modeling strategy applied in our recent study (Griffiths and Peltier 2008). As there, we use the most recent reconstruction of the LGM topography, the ICE-5G model of Peltier (2004), rather than the older ICE-4G model (Peltier 1996) used by most previous studies. Furthermore, our internal tide drag scheme uses a model-derived estimate of ocean stratification at LGM, rather than an ad hoc estimate. This is perhaps the first such estimate of LGM ocean stratification.

Although our solutions are global, we focus on changes in the polar tides. These changes are driven by the different polar coastal configuration at LGM, at which time ice sheets occupied the marginal seas of the present-day polar oceans. Polar tides have been neglected in recent high-resolution studies, some of which were unable to resolve the Arctic Ocean for numerical reasons, yet they are of special interest because of their interaction with adjoining ice shelves and ice streams. Furthermore, although the global sea level change at LGM is now well constrained by various data (Peltier and Fairbanks 2006), there remains uncertainty about the location and extent of marine ice sheets and shelves. Here, we shall explore the sensitivity of the polar tides to changes in these ice margins. Our simulations are ideally suited for this purpose, because they are performed on a global Mercator grid with enhanced resolution at high latitudes.

In the first half of our study we describe our modeling strategy in some detail. Our numerical global tide model is described in section 2. Key components are a new parameterization of internal tide drag, and a model of ocean stratification at LGM, which is required by this scheme. In section 3, we describe the global properties of the modeled tides, for present day and LGM, and examine their dependence upon model resolution and the internal tide drag scheme. In the second half of our study, we discuss polar tides. In section 4 we examine in detail the significant changes at LGM around the Antarctic coastline, and in section 5 we briefly discuss the changes around the Arctic coastline, extending the results of Griffiths and Peltier (2008). We conclude in section 6, by discussing the possibility of an interesting interplay between climate (which influences ice sheet extent) and polar tides (which influence ice sheet stability and the ocean circulation).

2. A global tide model

Writing the undisturbed ocean depth as H, the free-surface displacement as ζ, the depth-averaged horizontal flow as $\mathbf{u}$ and the corresponding volume transport as $\mathbf{U} = (H + \zeta)\,\mathbf{u}$, we model tides as a shallow-water flow:

$$\frac{\partial \mathbf{U}}{\partial t} = -\mathbf{f} \times \mathbf{U} - gH\nabla(\zeta - \zeta_{\mathrm{eq}} - \zeta_{\mathrm{sal}}) - \rho^{-1}H(\mathbf{D}_{\mathrm{BL}} + \mathbf{D}_{\mathrm{IT}}) \quad \text{and} \tag{1a}$$

$$\frac{\partial \zeta}{\partial t} = -\nabla \cdot \mathbf{U}. \tag{1b}$$

Here $\mathbf{f}$ is the vertical component of the Coriolis parameter, g is the acceleration due to gravity, ρ is a constant density for seawater, ζ_{eq} is the equilibrium tide representing astronomical forcing, and ζ_{sal} is the self-attraction and loading term (Hendershott 1972). Certain nonlinear terms are omitted from (1a), as in some other recent studies (e.g., Jayne and St. Laurent 2001; Egbert et al. 2004). The term $\mathbf{D}_{\mathrm{BL}}$ is a stress accounting for the drag of a turbulent bottom boundary layer, and is parameterized in the usual way (e.g., Taylor 1920) as

$$\mathbf{D}_{\mathrm{BL}} = \rho c_d |\mathbf{U}|\mathbf{U}/H^2, \quad \text{where } c_d = 0.0025.$$

The term $\mathbf{D}_{\mathrm{IT}}$, which parameterizes internal tide drag, is described in section 2c.

We solve these equations for forcing from a single tidal constituent of frequency ω. Our aim is to extract complex tidal coefficients $\hat{\mathbf{U}}$ and $\hat{\zeta}$ such that

$$\mathbf{U}(\mathbf{x},t) = \mathrm{Re}[\hat{\mathbf{U}}(\mathbf{x})e^{-i\omega t}], \quad \zeta(\mathbf{x},t) = \mathrm{Re}[\hat{\zeta}(\mathbf{x})e^{-i\omega t}].$$

Since the frictional term $\mathbf{D}_{\mathrm{BL}}$ is nonlinear, any solution inevitably involves terms of higher frequency, but these harmonics are small and not of interest here.

a. Numerical implementation

We use a spherical coordinate system with the model pole running through 75°N, 40°W (Greenland) and its antipode (Antarctica). We make a Mercator transformation within this rotated system, replacing latitude θ with a Mercacor latitude τ defined by $\tanh\tau = \sin\theta$. Solving on a regular Arakawa C grid in longitude and Mercator latitude τ, the effective latitudinal resolution increases poleward consistent with the convergence of meridians. At a typical resolution used here, with 720 points in each direction, the grid spacing smoothly varies from about 55 km in the tropics to 5 km around the coast of Greenland and in the Ross Sea.

The shallow-water equations (1a) and (1b) are integrated forward in time from rest. At the mth time step, $\mathbf{U}_m$ and ζ_m are advanced via

$$\tilde{\mathbf{U}}_{m+1} = \mathbf{U}_m + \Delta t\dot{\mathbf{U}}(\tilde{\mathbf{U}}_m, \zeta_m, t_m), \tag{2a}$$

$$\zeta_{m+1} = \zeta_m - \Delta t\,\nabla\cdot\left(\frac{\tilde{\mathbf{U}}_{m+1}+\mathbf{U}_m}{2}\right), \quad \text{and} \tag{2b}$$

$$\mathbf{U}_{m+1} = \mathbf{U}_m + \frac{\Delta t}{2}[\dot{\mathbf{U}}(\tilde{\mathbf{U}}_m,\zeta_m,t_m) + \dot{\mathbf{U}}(\tilde{\mathbf{U}}_{m+1},\zeta_{m+1},t_{m+1})], \tag{2c}$$

where $\dot{\mathbf{U}}$ includes all terms on the right-hand side of (1a). Note that by evaluating $\dot{\mathbf{U}}$ in (2a) and (2c) at the intermediate variable $\tilde{\mathbf{U}}_m$, rather than at $\mathbf{U}_m$, only one evaluation of $\dot{\mathbf{U}}$ is required per time step, the other being stored from the previous time step. (Equivalently, the Coriolis and drag terms can be treated using a second-order Adams–Bashforth scheme.) In addition to being second-order accurate in time, the major benefit of this scheme is that the maximum time step is *twice* the inverse of the maximum gravity wave frequency. Even so, the small grid spacing at high latitudes requires $\Delta t \le 30$ s at our standard resolution.

Each simulation is performed for a single tidal constituent of frequency ω. To reduce the excitation of transients, which is particularly important when modeling diurnal tides, the tidal forcing is premultiplied by a term $1 - \exp(-t^2/t_0^2)$, with $t_0 = 4$ days. Over the nth tidal period, a harmonic analysis is performed, yielding a tide $\zeta^{(n)}(\mathbf{x},t) = \mathrm{Re}[\hat{\zeta}^{(n)}(\mathbf{x})\exp(-i\omega t)]$. The integration is terminated when equilibrium is reached, typically after about 20 days, when the global average of $||\hat{\zeta}^{(n)}| - |\hat{\zeta}^{(n-1)}||$ is a few millimeters.

During the $(n+1)$th tidal period, the self-attraction and loading term is implemented as

$$\zeta_{\mathrm{sal}} = \beta^{(n)}\zeta + \mathrm{Re}\{[\hat{\zeta}^{(n)}_{\mathrm{sal}} - \beta^{(n)}\hat{\zeta}^{(n)}]\exp(-i\omega t)\},$$

where $\hat{\zeta}^{(n)}_{\mathrm{sal}}$ is calculated from $\hat{\zeta}^{(n)}$ using a spherical harmonic transform with load Love numbers obtained from Farrell (1973), and

$$\beta^{(n)}(\mathbf{x}) = \mathrm{Re}\left[\frac{\int \hat{\zeta}^{(n)}_{\mathrm{sal}}\hat{\zeta}^{(n)*}\,dA}{\int \hat{\zeta}^{(n)}\hat{\zeta}^{(n)*}\,dA}\right].$$

Here, the integration is typically performed over gridpoints within 3° (in longitude and Mercator latitude) of $\mathbf{x}$, and the resulting values are confined to the range $0 \le \beta^{(n)} \le 0.3$. This implementation is similar to those used by Egbert et al. (2004) and Arbic et al. (2004a), although we find that a spatially varying parameter $\beta^{(n)}$ leads to a more reliable convergence in $\hat{\zeta}^{(n)}$.

b. Bathymetry

For the present-day simulations, H is constructed from a modified version of the 2-minute gridded elevations/bathymetry for the world (ETOPO2) dataset. For LGM, H is interpolated from the ICE-5G v. 1.3 dataset for 26 000 yr before present, which is based on the same 2-min topography but accounts for both the water taken up by the ice sheets, and the deformation of the earth beneath the ice sheets. This is an updated version of the widely used ICE-5G v 1.2 dataset (Peltier 2004). The locations of the continents and ice sheets for both present day and LGM are shown in Fig. 1. At LGM there are significant changes in the coastal configurations of the Arctic, North Atlantic, and western Pacific Oceans.

In our tidal modeling, no account is taken of floating ice shelves such as those that exist around much of present-day Antarctica. These imply a reduction in the ocean depth and an additional drag on the flow due to a turbulent boundary layer at the water–ice interface. The omission of these effects does not appear to degrade the present-day global solutions, perhaps because the extent of the ice shelves is small. At LGM, the extent of ice shelves was presumably much larger than at present, but to what degree is not well known. We thus solely examine the effects due to sea level drop and changes in

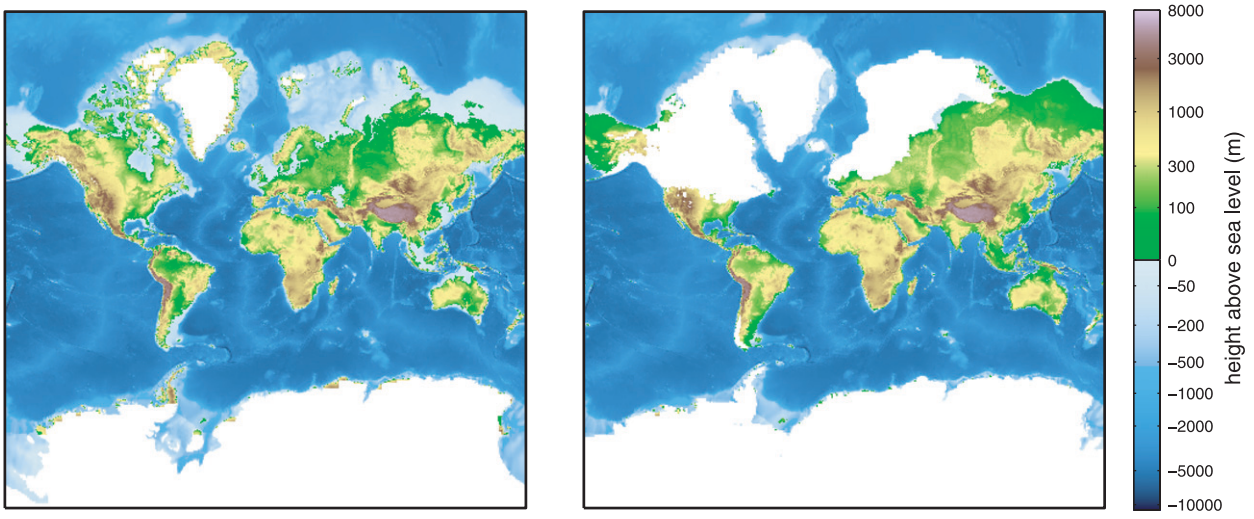

FIG. 1. Surface height (m) and ice location of the ICE-5G v 1.3 reconstruction for (left) present day and (right) LGM.

coastal geometry, which are well constrained, and that are likely to be responsible for the largest changes in the global tides.

c. Internal tide drag

As the tide flows over topography, internal waves of tidal frequency are generated wherever the ocean is density stratified. Density perturbations associated with the internal tide create a pressure perturbation p_{IT} at the ocean floor $z = -H$, which implies a downward stress with horizontal component $-p_{\mathrm{IT}}\nabla H$. The equal and opposite upward stress implies a drag

$$\mathbf{D}_{\mathrm{IT}} = -p_{\mathrm{IT}}\nabla H, \tag{3}$$

which acts on the depth-averaged flow in (1a). Dynamically, $\mathbf{D}_{\mathrm{IT}}$ modifies tidal flows in the open ocean, where $\mathbf{D}_{\mathrm{BL}}$ is weak. Furthermore, since energy is extracted from the depth-averaged flow at a rate $\mathbf{u}\cdot\mathbf{D}_{\mathrm{IT}}$, there is an internal tide dissipation whenever the time average of this quantity is positive.

The internal tide drag $\mathbf{D}_{\mathrm{IT}}$ would be explicitly calculated in a baroclinic tidal model, such as that of Simmons et al. (2004). However, in a barotropic tidal model such as (1a) and (1b), p_{IT} must be parameterized. Unfortunately, no simple expressions exist for p_{IT}, which is a nonlocal function of the surrounding flow and topography. Furthermore, small- and large-amplitude topography are expected to lead to quite different expressions for p_{IT}. We use a simple scaling argument to estimate p_{IT} for flow over large-amplitude topography, such as that resolved by our model bathymetry. The hydrostatic relationship implies

$$p_{\mathrm{IT}} = -g\int_{-H}^{0}\rho_{\mathrm{IT}}\,dz \sim g\rho_{\mathrm{IT}}H_{\mathrm{IT}},$$

where ρ_{IT} is the density perturbation of the internal tide, and where $H_{\mathrm{IT}} < H$ is the vertical length scale over which the wave field is coherent. At the ocean floor the vertical velocity $w = -\mathbf{u}\cdot\nabla H$, so for a tide of frequency ω one expects vertical displacements $\Delta z \sim \mathbf{u}\cdot\nabla H/\omega$. Since $\rho_{\mathrm{IT}} \sim \Delta z\,\partial\rho/\partial z \sim \rho\overline{N}^2\Delta z/g$, where $\overline{N}$ is the buoyancy frequency, we estimate

$$p_{\mathrm{IT}} \sim \rho\overline{N}^2 H_{\mathrm{IT}}\mathbf{u}\cdot\nabla H/\omega. \tag{4}$$

For internal tide generation by large topographic features, which is dominated by the low-order baroclinic modes, we expect $H_{\mathrm{IT}} \sim H$. We take $H_{\mathrm{IT}} = H/3$, this particular choice being motivated by asymptotic solutions of the baroclinic modal equations of Griffiths and Grimshaw (2007). Furthermore, since the density perturbations extend throughout the fluid column for low-order baroclinic modes, we take

$$\overline{N} = \frac{1}{H}\int_{-H}^{0} N(z)\,dz.$$

This column-averaged stratification will overestimate the internal wave drag if the value of $\overline{N}$ at the ocean floor is a more relevant parameter.

We thus obtain a completely local estimate of the magnitude of baroclinic pressure perturbations at the ocean floor. To complete our parameterization, we recall that the internal tide is trapped around the topography if $|f| > \omega$. Since no freely propagating waves are then generated, p_{IT} is necessarily out of phase with $\mathbf{u}$ and the time average of $\mathbf{u}\cdot\mathbf{D}_{\mathrm{IT}}$ is zero, at least in the

linear regime. If $|f| < \omega$, freely propagating waves are generated, and p_{IT} has components that are both in phase and out of phase with the **u**. Tidal models usually only parameterize the in-phase component of p_{IT}, since only this contributes to the dissipation. We follow this convention, but note that the out-of-phase component of p_{IT} may have dynamical significance that is not presently accounted for. We therefore simply combine (3) and (4) to give

$$\mathbf{D}_{\mathrm{IT}} = \frac{\rho \overline{N}^2}{3\omega}(H\mathbf{u}\cdot\nabla H)\nabla H \times \begin{cases} 1 & \text{for} \quad |f| < \omega, \\ 0 & \text{for} \quad |f| > \omega. \end{cases} \tag{5}$$

We have chosen the sign so that $\mathbf{u} \cdot \mathbf{D}_{\mathrm{IT}} \geq 0$, corresponding to the generation of internal waves and an extraction of energy from the depth-averaged flow. Our parameterization is designed to account for internal wave generation by large steep topographic features, such as midocean ridges and continental slopes, which are resolved by our topographic dataset. It will typically overestimate dissipation by any resolved small-amplitude topography. We do not account for any internal tide drag due to unresolved topography.

This parameterization is similar to that used by Carrère and Lyard (2003) and Lyard et al. (2006), in that (i) $\mathbf{D}_{\mathrm{IT}}$ is proportional to $\mathbf{u} \cdot \nabla H$, so that there is no drag for along-slope flow, and (ii) $\mathbf{D}_{\mathrm{IT}}$ is directed normal to the slope, consistent with the most basic physical relationship in (3). However, in contrast to their scheme and others, such as that of Jayne and St. Laurent (2001), (5) has no free parameters. We will discuss the significance of this in section 3c.

d. Stratification

To implement (5), estimates of the vertically averaged buoyancy frequency $\overline{N}$ are required. For the present-day ocean, $\overline{N}$ can be estimated from observations. However, this cannot be done for LGM, because data, such as the few estimates of temperature and salinity in the deep ocean given by Adkins et al. (2002), is too sparse. This is an important issue, because the shallow marginal seas almost entirely disappear at LGM, as shown in Fig. 1. Thus, $\mathbf{D}_{\mathrm{BL}}$ provides less drag, so that internal tide drag is thought to play a major role in setting LGM tidal amplitudes and dissipation (Egbert et al. 2004; Wunsch 2005).

However, it is also possible to estimate ocean stratification from suitably sophisticated coupled atmosphere–ocean climate simulations. Here we analyze output from the simulations of Peltier and Solheim (2004), which were performed for both present-day and LGM conditions. They ran the Climate System Model version 1.4 (CSM 1.4) to equilibrium over a period of 2000 yr, resolving the ocean with 25 vertical levels and a 116×102 latitude–longitude grid. Time-averaged temperature, salinity, and buoyancy frequency were calculated from the final 50 yr of these simulations. Latitude–height cross sections of these quantities, running through the Atlantic and then into the Arctic Ocean, are shown in Fig. 2.

The present-day simulation captures many features of the real ocean. For instance, note the thermocline at a depth of about 50 m, the formation of Antarctic bottom water (seen most clearly in the temperature), and the formation of Antarctic intermediate water (seen most clearly in the salinity). The most serious deficiency is a surface freshwater bias in the tropics, caused by a well-known drift in CSM 1.4. This typically leads to buoyancy frequencies which are too high relative to those calculated from the World Ocean Atlas dataset (Antonov et al. 2006; Locarnini et al. 2006), as will be discussed shortly.

At LGM, generally the ocean is cooler and saltier, with an estimated average increase in salinity of 3.7% due to the 3.6% reduction in the volume of the ocean. Nevertheless, the buoyancy frequency remains largely unchanged over much of the ocean. This is consistent with the results of Adkins et al. (2002), where deep salinity increases of $2.7 \pm 0.1\%$, $3.3 \pm 0.3\%$, $4.2 \pm 0.2\%$ and $6.9 \pm 0.5\%$ were reported at LGM. These increases need not imply a generally fresher upper ocean and larger stratification, since only in the final case is the salinity increase anomalously large. Two regions of the CSM 1.4 results deserve special mention. First, around Antarctica, there is increased bottom-water formation, driven by increases in sea ice. The enhanced vertical mixing associated with this leads to a more homogeneous water column, and lower buoyancy frequencies. Second, in the Greenland Sea and Arctic Ocean, the buoyancy frequency is higher than at present. This again appears to be driven by enhanced sea ice formation, which leads to an accumulation of salt in the deep Arctic Ocean. Unlike the Southern Hemisphere, this salty water cannot readily escape into the Atlantic because of the relatively shallow water around Iceland.

The vertically averaged buoyancy frequency $\overline{N}$, which is used by the internal tide drag scheme, is shown in Fig. 3 for both present day and LGM. Much of the spatial variation of $\overline{N}$ simply correlates with ocean depth, with large values of $\overline{N}$ in the shallow marginal seas, and smaller values in the deep ocean. Horizontal averages of $\overline{N}$ for individual oceans are given in Table 1. As shown there, the present-day CSM 1.4 simulations overestimate $\overline{N}$ when measured against values calculated from the World Ocean Atlas. At LGM, the simulations

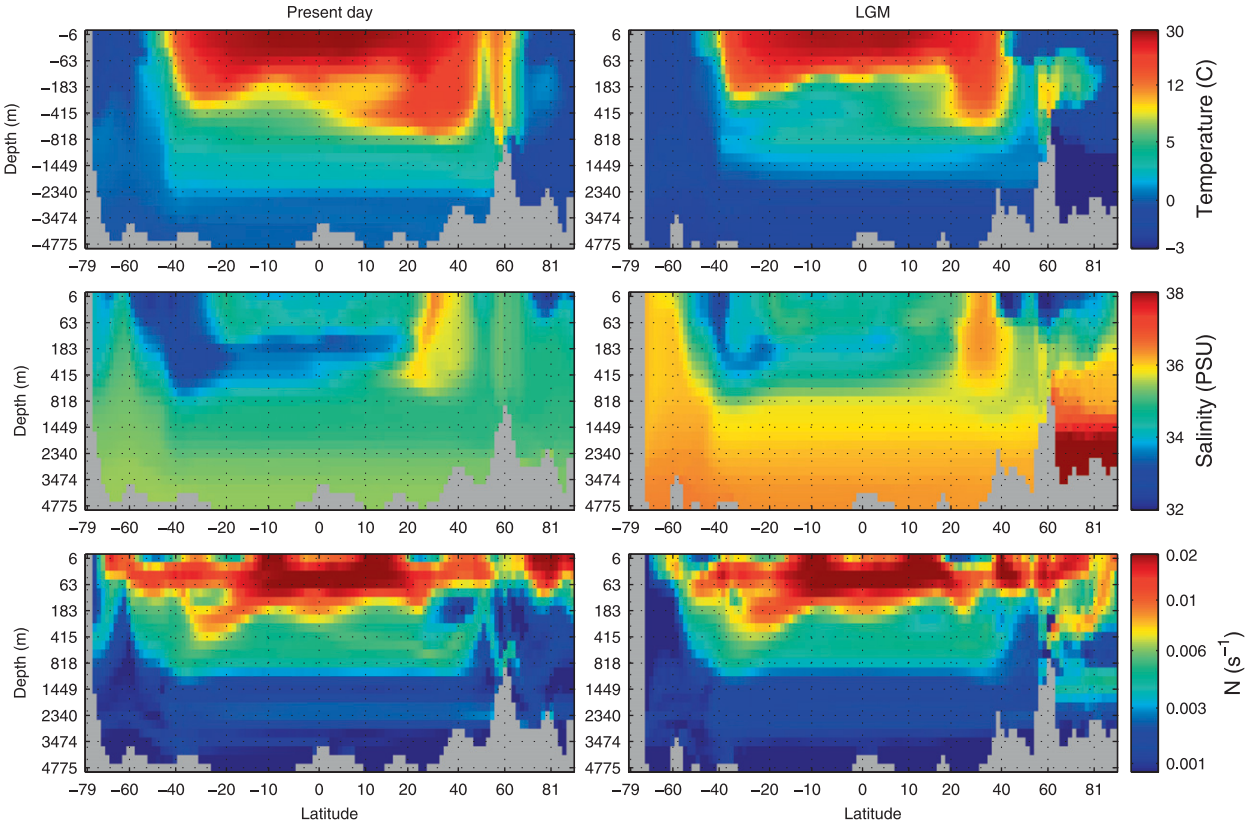

FIG. 2. Temperature, salinity, and buoyancy frequency N of the Atlantic and Arctic Oceans according to the results of Peltier and Solheim (2004). The longitudinal positioning of the cross section is shown by the dashed line in Fig. 3. Quantities are displayed on a nonuniform vertical and latitudinal grid, which is that used by the ocean model of Peltier and Solheim.

predict a fall in $\overline{N}$ of about 10% over the Pacific and Indian Oceans, and about 20% over the Southern Ocean. In contrast, $\overline{N}$ is predicted to increase by 70% in the Arctic Ocean, for the reasons noted above. This increased stratification could play a role in moderating semidiurnal tides, although the latitudinal extent of the drag is limited by (5) (e.g., equatorward of 74° for the dominant semidiurnal constituent M_2).

Although there are certain to be errors in these model-derived buoyancy frequencies, we apply a consistent approach by using these values for both the present-day and LGM tidal simulations. This is in contrast to previous studies, in which LGM stratification was typically set to present-day values, or to a multiple of present-day values. With the exception of some simulations presented in section 3c to illustrate model sensitivity, we adopt these model-derived buoyancy frequencies exclusively.

3. Global tides

We focus on the largest semidiurnal tidal constituent (M_2, of frequency $\omega = 1.405 \times 10^{-4}\ \mathrm{s}^{-1}$) and the largest diurnal constituent (K_1, of frequency $\omega = 7.292 \times 10^{-5}\ \mathrm{s}^{-1}$), which account for 68% and 11% of the tidal energy in the present-day ocean (Egbert and Ray 2003). The observed amplitudes of these components are shown in Figs. 4a,b, as described by the complex amplitude $\hat{\zeta}_{\mathrm{tp}}$ of the TPXO 6.2 dataset, an updated version of the data-constrained solutions described by Egbert et al. (1994). As is well known, semidiurnal tides are large in the North Atlantic, while diurnal tides are large in the North Pacific, due to near resonances with the ocean depth and coastal configuration (e.g., Platzman 1984).

Our numerically determined solutions for the present-day ocean are shown in Figs. 4c,d. These were calculated on a 1080×1080 grid, which corresponds to a globally averaged grid spacing of 30 km (or 0.27° at the equator). Comparing with the TPXO 6.2 solutions, it is clear that the M_2 and K_1 amplitudes are well reproduced by our numerical model. The M_2 tide is too large in the North Atlantic, while the only deficiency in the K_1 solution is a westward extension of the large tides in the Sea of Okhotsk. We quantify the average global error against a reference tide $\hat{\zeta}_{\mathrm{ref}}$ via

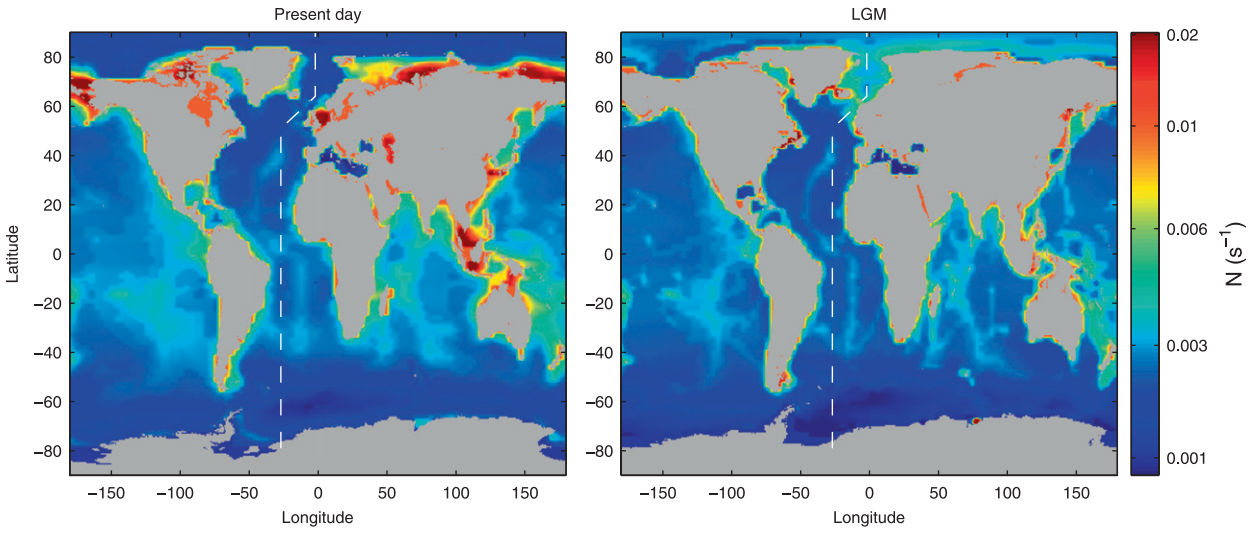

FIG. 3. Vertically averaged buoyancy frequency $\overline{N}$, derived from the results of Peltier and Solheim (2004). In any regions not resolved by their model, such as present-day Hudson Bay and several marginal seas, we have set $\overline{N} = 0.01\,\mathrm{s}^{-1}$.

$$\overline{\Delta\zeta} = \sqrt{\frac{\int |\hat{\zeta} - \hat{\zeta}_{\mathrm{ref}}|^2 dA}{2\int dA}}, \tag{6}$$

which takes into account errors in both amplitude and phase. This is equivalent to the time-averaged expression used by Arbic et al. (2004a), and others. We take $\hat{\zeta}_{\mathrm{ref}} = \hat{\zeta}_{\mathrm{tp}}$ (the TPXO 6.2 solution), and evaluate the integrals equatorward of 66° (where $\hat{\zeta}_{\mathrm{tp}}$ is most reliable) and in waters deeper than 1000 m, as is traditional. Then, the M_2 and K_1 solutions of Figs. 4c,d have $\overline{\Delta\zeta} = 11.8$ cm and 2.8 cm, respectively. Evaluating the corresponding signals via

$$\overline{\zeta} = \sqrt{\frac{\int |\hat{\zeta}_{\mathrm{tp}}|^2 dA}{2\int dA}},$$

giving $\overline{\zeta} = 26.5$ cm for M_2 and $\overline{\zeta} = 9.5$ cm for K_1, we can evaluate the fraction of sea surface height variance captured by our model (equal to $1 - \overline{\Delta\zeta}^2/\overline{\zeta}^2$). We obtain 80.2% for M_2 and 91.3% for K_1, a little less than the values given in Table 2 of Arbic et al. (2004a).

Corresponding numerically determined solutions for LGM are shown in Figs. 4e,f. Although the pattern of the M_2 tide remains similar, the amplitude is typically enhanced relative to the present-day solution (such as around New Zealand and off the east coast of Brazil). The amplification in the North Atlantic has been modeled previously (Egbert et al. 2004; Arbic et al. 2004b), and discussed in some detail by Uehara et al. (2006) and Arbic et al. (2008). Later, we shall discuss the amplified M_2 tide in the Weddell Sea, visible at about 50°W on the Antarctic coastline. Evaluating (6) for the LGM M_2 tide, taking the modeled present-day tide for $\hat{\zeta}_{\mathrm{ref}}$ gives $\overline{\Delta\zeta} = 31.2$ cm, almost 3 times the present-day error. In contrast, the K_1 tide is relatively unchanged at LGM, with $\overline{\Delta\zeta} = 3.7$ cm when measured against the modeled present-day tide, of the same order as the present-day error. Locally, the two main differences for K_1 are the amplification in the South China Sea, noted by Uehara (2005), and the amplified tide encircling Antarctica.

TABLE 1. Horizontally averaged $\overline{N}$ for the World Ocean Atlas (WOA) dataset, the CSM 1.4 present-day simulations (MOD), and the CSM 1.4 LGM simulations. Also given are RMS differences $\Delta\overline{N}$ between the two present-day datasets and the two CSM 1.4 datasets. All averages are taken over waters deeper than 1000 m, where internal tide drag is most important.

	Horizontally averaged $\overline{N}(\times 10^{-3}\mathrm{s}^{-1})$			RMS difference $\Delta\overline{N}(\times 10^{-3}\mathrm{s}^{-1})$	
Ocean	WOA	MOD	LGM	WOA vs MOD	MOD vs LGM
Southern	1.08	1.81	1.49	0.783	0.446
Arctic	1.49	1.79	3.01	0.642	1.396
Indian	2.19	3.32	2.97	1.242	0.561
Pacific	2.05	3.11	2.82	1.169	0.462
Atlantic	1.82	2.64	2.45	0.899	0.498

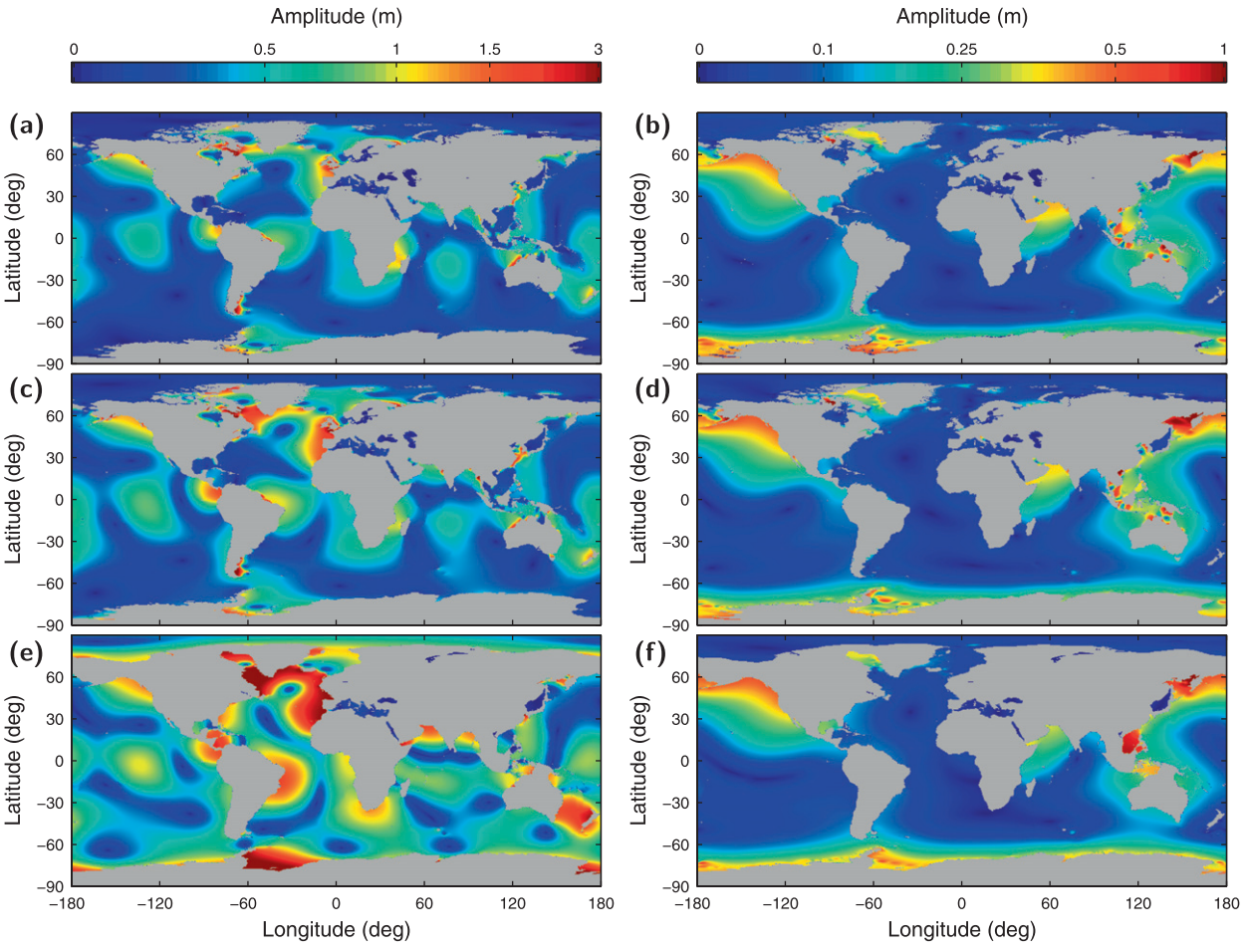

FIG. 4. Tidal amplitudes for the (left) M_2 and (right) K_1 constituents from (top) the TPXO 6.2 dataset, (middle) the present-day model with $M = 1080$, and (bottom) the LGM model with $M = 1080$.

Note that the M_2 component is similarly amplified along the entire coastline of the Arctic Ocean. We shall discuss these changes in sections 4 and 5.

a. Effects of model resolution

As is evident from Figs. 4a–d, the present-day modeled tides are too energetic, at least relative to the observationally constrained TPXO 6.2 solutions. This effect can largely be attributed to model resolution. To illustrate this, we have calculated M_2 and K_1 tidal solutions at a range of model resolutions, with the number of longitudinal grid points varying from $M = 270$ to $M = 1080$. The calculated energies are shown in Figs. 5a,b, along with the values given by Egbert and Ray (2003) for corresponding TPXO solutions. One can see that the energy decreases as the model resolution increases, for both present-day and LGM simulations. Indeed, the energies of modeled present-day tides appear to be approaching the observed values, but even at $M = 1080$ the energy is overestimated by 50% for M_2 and 30% for K_1. Egbert et al. (2004) demonstrated that better agreement can be obtained at yet higher resolution (see their Fig. 2b), whether or not one is using an internal-tide drag scheme. Some related results are given in appendix A of Simmons et al. (2004).

It is not surprising that the solutions should become more accurate as the resolution increases. For instance, the accuracy of the finite-difference approximations will improve leading to a better treatment of highly sensitive near-resonant modes, and the model grid will better resolve key coastal features and channels. Such effects can occasionally lead to large improvements in the solution for only a small increase in resolution, such as apparently occurs for the LGM M_2 tide around $M = 450$. However, it is somewhat surprising that the energy should always be overestimated at finite resolution. This behavior is consistent with the presence of a dissipative process within (1a) and (1b), which acts more effectively at high model resolution. We discount internal tide drag as being the dominant such process, since E

TABLE 2. Sensitivity of modeled tides to the internal tide drag scheme for both present-day (MOD) and LGM simulations at $M = 720$. Given are the global energy E, the parameterized boundary layer dissipation D_{BL}, internal tide dissipation D_{IT}, total dissipation D, and average global error $\overline{\Delta\zeta}$. Also given are the corresponding values for the TPXO.5 global assimilation solution, taken from Table 1 of Egbert and Ray (2003).

Tide	Era	Setting	E (PJ)	D_{BL} (TW)	D_{IT} (TW)	D (TW)	$\overline{\Delta\zeta}$ (cm)
M_2	MOD	TPXO.5	312	1.65	0.78	2.44	—
M_2	MOD	Standard $\mathbf{D}_{IT}$	588	2.27	1.14	3.41	13.7
M_2	MOD	Global $\mathbf{D}_{IT}$	586	2.26	1.15	3.41	13.6
M_2	MOD	$4 \times \mathbf{D}_{IT}$	356	1.08	2.05	3.12	9.81
M_2	LGM	Standard $\mathbf{D}_{IT}$	1167	1.17	2.74	3.92	—
M_2	LGM	Global $\mathbf{D}_{IT}$	1157	1.15	2.77	3.92	—
M_2	LGM	$4 \times \mathbf{D}_{IT}$	625	0.42	3.29	3.71	—
K_1	MOD	TPXO.5	50	0.30	0.04	0.34	—
K_1	MOD	Standard $\mathbf{D}_{IT}$	77	0.24	0.13	0.37	3.12
K_1	MOD	Global $\mathbf{D}_{IT}$	60	0.14	0.23	0.37	2.76
K_1	MOD	$4 \times \mathbf{D}_{IT}$	63	0.16	0.21	0.37	3.98
K_1	LGM	Standard $\mathbf{D}_{IT}$	66	0.09	0.16	0.25	—
K_1	LGM	Global $\mathbf{D}_{IT}$	57	0.05	0.23	0.28	—
K_1	LGM	$4 \times \mathbf{D}_{IT}$	49	0.08	0.25	0.33	—

also falls with resolution when $\mathbf{D}_{IT}$ is omitted from the formulation. Other possibilities are (i) small-scale bottom roughness and coastal roughness, which leads to a greater scattering of the tide as the resolution increases, reducing its coherency and energy; and (ii) bottom friction, which might become more effective as shallow regions and narrow channels with vigorous flow are better resolved. Either way, note that a higher effective drag need not lead to a higher dissipation D, for the reasons explained by Platzman (1984, his Fig. 1) and Egbert et al. (2004, their Fig. 11). Thus, even though D may increase with resolution in some cases, in others it may fall (e.g., Fig. 5c, modern) or level off (e.g., Fig. 5d, modern).

b. Energetics

It is clear from Figs. 5a,b that the energy of the M_2 tide approximately doubles at LGM, while that of the K_1 tide stays about the same. However, perhaps of greater

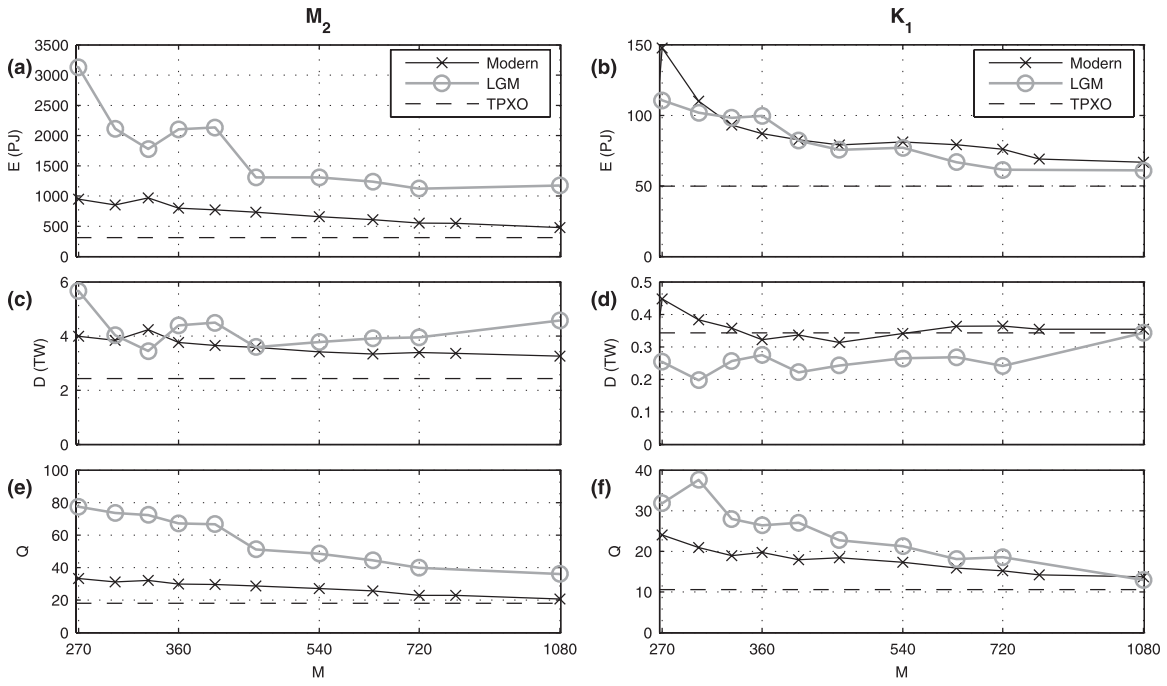

FIG. 5. The effects of model resolution (measured by the number of longitudinal grid points M) on global energy E, total dissipation D, and response quality $Q = \omega E/D$.

interest is how the dissipation D changes. We decompose this as $D = D_{\mathrm{BL}} + D_{\mathrm{IT}}$, where

$$D_{\mathrm{BL}} = \langle \mathbf{u} \cdot \mathbf{D}_{\mathrm{BL}} \rangle, \quad D_{\mathrm{IT}} = \langle \mathbf{u} \cdot \mathbf{D}_{\mathrm{IT}} \rangle,$$

the angled brackets denoting a time average over one tidal period. From D, and the energy E, we also calculate the response quality $Q = \omega E/D$.

For the present-day M_2 tide, as the resolution increases D appears to be approaching the 2.44 TW quoted by Egbert and Ray (2003), as shown in Fig. 5c. At $M = 1080$, we have $\mathbf{D}_{\mathrm{BL}} = 1.90$ TW and $\mathbf{D}_{\mathrm{IT}} = 1.38$ TW, so that 42% of the dissipation is accounted for by internal tide drag. A slightly lower amount (36%) of the dissipation occurs in waters deeper than 1000 m, consistent with the 32% quoted by Egbert and Ray (2003). In contrast, for the K_1 component, the present-day dissipation appears to have converged to about the correct value even at the low resolution of $M = 360$. At $M = 1080$, we have $\mathbf{D}_{\mathrm{BL}} = 0.20$ TW and $\mathbf{D}_{\mathrm{IT}} = 0.16$ TW, so that 44% of the dissipation is accounted for by internal tide drag. Here 39% of the dissipation occurs in the waters deeper than 1000 m, which is considerably larger than the 11% quoted by Egbert and Ray (2003).

At LGM, we find little change in the dissipation of the K_1 constituent, consistent with the results of Egbert et al. (2004). However, the M_2 tide appears to be approaching a state with D in excess of 4 TW, considerably higher than the 2.44 TW of the present-day ocean. This is consistent with the values estimated by Egbert et al. (2004) and Uehara et al. (2006). For both M_2 and K_1, the bulk of the dissipation is now accounted for by internal tide generation in the deep ocean. For M_2, the proportion is 63%, while for K_1 the proportion is 57%. In each case, this represents an approximate reversal of the dissipation split for the present-day modeled tides, consistent with the expectation that internal tide drag is the dominant dissipation mechanism at LGM. This energy is potentially available to drive enhanced vertical mixing in the deep ocean (e.g., Montenegro et al. 2007).

c. Internal tide drag: Sensitivity and tuning

As already noted in section 3a, at the resolutions typically used by global tide models, that is about 0.25°–0.5°, it seems that an untuned model will typically overestimate tidal energies. This problem is often ''remedied'' by increasing dissipation aphysically, for instance by adding and tuning a horizontal viscosity, as in Thomas and Sündermann (1999). Alternatively, Arbic et al. (2004a) demonstrated that errors in the present-day M_2 tide can be minimized by increasing the drag coefficient c_d in $\mathbf{D}_{\mathrm{BL}}$. They found that $c_d = 0.64$ was optimal for their model, and noted this as being unrealistically large. However, since horizontal viscosity has no physical basis here and c_d is thought to be well-constrained, tidal solutions are instead often improved by increasing the parameterized internal tide drag $\mathbf{D}_{\mathrm{IT}}$, perhaps simply by tuning a multiplicative constant (e.g., Jayne and St. Laurent 2001; Arbic et al. 2004a). It is then argued that such tuning merely corrects for deficiencies in the parameterization of internal tide drag, since the simple expressions used for $\mathbf{D}_{\mathrm{IT}}$ are crude and poorly constrained. Note that the optimal tuning is resolution dependent (Arbic et al. 2008).

We illustrate the consequences of this procedure by presenting additional simulations (at $M = 720$) with enhanced internal tide drag, for both present day and LGM. We first simply apply (5) globally, rather than in the restricted latitude band with $|f| < \omega$. Physically, this might account for drag due to the generation of nonlinear internal waves or baroclinic edge waves, which can occur at high latitudes. As shown in Table 2, this only leads to changes in the K_1 tide, with the M_2 tide remaining almost unchanged for both present day and LGM. This is not unexpected, because the region of additional drag (where $|f| > \omega$) is much larger for diurnal tides than for semidiurnal tides. For the present-day K_1 tide, the additional drag does reduce the energy toward the observed value, and $\overline{\Delta\zeta}$ falls by a modest 12%. However, this cannot be regarded as a more physically consistent solution since the modeled internal tide dissipation becomes unrealistically large. Thus, applying internal tide drag globally does not lead to improved solutions.

In our second set of sensitivity simulations, we multiply the right-hand side of (5) by a factor of 4, which corresponds to increasing the parameter H_{IT} in (4) from $H/3$ to $4H/3$. Physically, this might account for an underestimate of the internal wave drag by our standard parameterization in (5). As shown in Table 2, this does lead to an improved present-day M_2 solution, when measured in terms of energy and $\overline{\Delta\zeta}$. However, this is again achieved at the cost of a solution with unrealistically large internal tide dissipation: $D_{\mathrm{IT}} \approx 2 \times D_{\mathrm{BL}}$, in contrast to observations with $D_{\mathrm{IT}} \approx 0.5 \times D_{\mathrm{BL}}$. For the present-day K_1 solution, the enhanced internal tide drag reduces the energy toward the observed value, but $\overline{\Delta\zeta}$ increases, and there is the same problem with unrealistically large internal tide dissipation. We conclude that enhancing the internal tide drag does not lead to more physically consistent solutions, even though tidal energies are reduced toward observed values.

Putting aside this problem of unrealistically large internal tide dissipation, such tuning is hard to justify in the context of the convergence demonstrated in Figs. 5a,b (and in Fig. 2b of Egbert et al. 2004). Furthermore, the

amount of tuning required will clearly depend upon the tidal constituent, the configuration of the coastline, and the stratification of the ocean. Thus, it is dangerous to tune the internal tide drag to fit present-day tides and then to use the same parameterization to model tides at LGM. We prefer our modeled tides to be too energetic, and to interpret them in terms of the convergence shown in Figs. 5a,b. Furthermore, in this study we are most interested in tidal amplitudes, and a 30%–50% overestimate in energy implies that tidal amplitudes are only overestimated by 15%–20%.

The second set of sensitivity simulations, with $\mathbf{D}_{\mathrm{IT}}$ increased by a factor of 4, can alternatively be interpreted as results for an ocean with $\overline{N}$ increased by a factor of 2. Since the stratification of the LGM ocean is unknown, these results can be used to gauge the uncertainty of our global tidal solutions. As can be seen in Table 2, the dominant effect is to reduce the energy of the LGM tides, with the M_2 tidal energy falling by almost 50%. This is consistent with corresponding sensitivity studies made by Egbert et al. (2004) and Arbic et al. (2008). Those authors also considered the effects of reduced stratification, and discussed changes from a more regional perspective. Note that total dissipation D need not increase as the internal tide drag increases, for the reasons noted at the end of section 3a.

4. Antarctic tides

a. The K_1 tide

More detailed views of the modeled K_1 tides around Antarctica (calculated using $M = 720$) are shown in Fig. 6. The modern-day amplitude (Fig. 6a) takes an approximately annular structure around the coastline, superposed with various other features around the shelf-break and in the semienclosed Ross and Weddell Seas. Along the coastline (Fig. 7), the annular structure has an amplitude of about 30 cm, while the Ross Sea tides reach an amplitude of about 75 cm. Snapshots of the tide separated by one-quarter of a tidal period (Figs. 6b,c) clearly show that the annular structure corresponds to a zonal wavenumber 1 Kelvin wave, propagating anticyclonically, as expected from standard theory (e.g., Gill 1982).

A simple model of this tide can be developed by considering free wave propagation around a zonally symmetric polar continent. Omitting the forcing and dissipation from (1a) and (1b), and seeking Kelvin wave solutions by setting the meridional velocity to be 0, we have

$$\frac{\partial U}{\partial t} = -\frac{gH}{r\cos\theta}\frac{\partial \zeta}{\partial \phi}, \tag{7a}$$

$$2\Omega \sin\theta\, U = -\frac{gH}{r}\frac{\partial \zeta}{\partial \theta}, \quad \text{and} \tag{7b}$$

$$\frac{\partial \zeta}{\partial t} + \frac{1}{r\cos\theta}\frac{\partial U}{\partial \phi} = 0, \tag{7c}$$

where θ is latitude, ϕ is longitude, U is the zonal transport velocity, and r is the earth's radius. Placing the continental boundary at $\theta = \theta_0$, and taking an ocean of depth

$$H = H_0\left(\frac{\cos\theta}{\cos\theta_0}\right)^2, \tag{8}$$

(7a) and (7c) can be combined to give a simple wave equation for U or ζ, with solutions

$$\begin{pmatrix} U \\ \zeta \end{pmatrix} = \mathrm{Re}\left[\begin{pmatrix} r\omega_n \cos\theta \\ \pm n \end{pmatrix} A_{\pm}(\theta) e^{i(n\phi \mp \omega_n t)}\right], \tag{9}$$

where n is an integer (to ensure periodicity), and

$$\omega_n = \frac{n\sqrt{gH_0}}{r\cos\theta_0}. \tag{10}$$

The functions $A_{\pm}(\theta)$ are then determined from (7b):

$$A_{\pm}(\theta) = A_0\left(\frac{\cos\theta}{\cos\theta_0}\right)^{\pm 2\Omega r\cos\theta_0/\sqrt{gH_0}}. \tag{11}$$

Since we wish to find an edge wave that decays equatorward away from the polar coastline, we must take the solution proportional to $A_{-}(\theta)$. From (9), this corresponds to a westward-traveling wave [i.e., one with the coast on the right (left) in the northern (southern) hemisphere] as expected.

To apply this theory to Antarctica, we take $H_0 = 2000$ m and $\theta = 70°$, so that (10) implies $\omega_1 = 6 \times 10^{-5}$ s^{-1}. Thus, the zonal wavenumber-1 Kelvin wave is close to resonance at diurnal frequencies, accounting for its strong signature in Figs. 6a–c. This same idea is implicit in the analysis of Platzman et al. (1981), who calculated that Antarctica has a normal mode of period 29 h, taking the form of a Kelvin wave with zonal wavenumber 1.

At LGM, the coastal margins of Antarctica were quite different, as ice sheets flowed out from the mainland to partially occupy the continental shelves. In the ICE–5G v 1.3 reconstruction, the ice sheets extend to approximately midshelf in both the Ross and Weddell Seas (cf. the black and blue areas shown in Fig. 8). As a result, the Antarctic coastline becomes considerably smoother. One would expect this to promote the free passage of Kelvin waves, since there will be less scattering from sharp coastal features, and shallow areas of strong dissipation are reduced in size. This expectation is confirmed by our

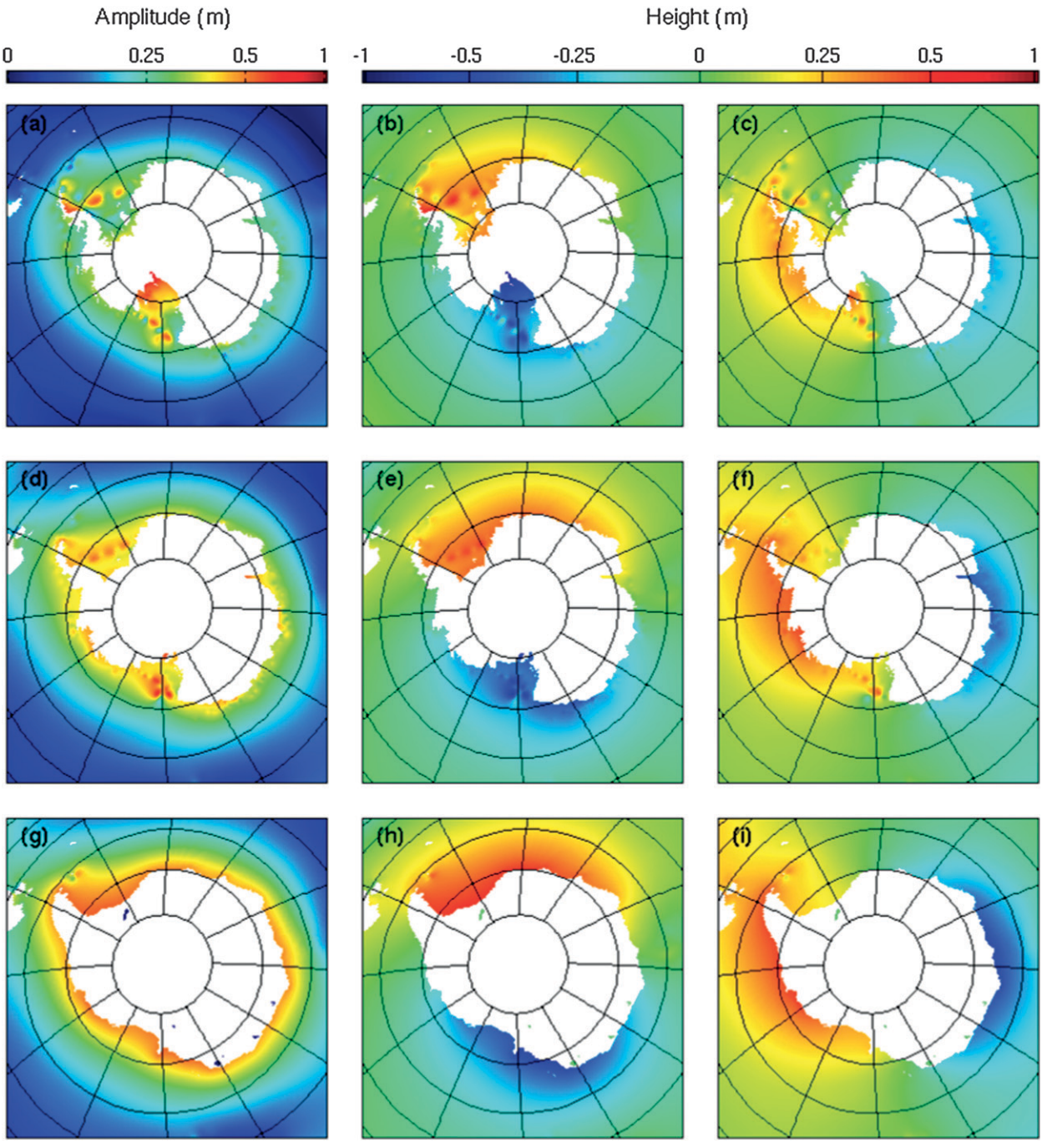

FIG. 6. The K_1 tides (calculated at $M = 720$) for the (top) present-day model, (middle) LGM model, and (bottom) LGM 60 model with grounded ice occupying the entire continental shelf. (middle), (right) Instantaneous snapshots of the tide separated by one-quarter of a tidal period.

simulations (Figs. 6d–f). At LGM the structure of the K_1 tide is rather similar to that of the present-day tide, but there is an amplification around the entire continent (also see Fig. 7).

However, just how much of the continental shelves was occupied by grounded ice sheets at LGM is not precisely known. We have therefore explored other scenarios, as shown in Fig. 8, in which ice sheets extend farther out toward the continental shelf break. These configurations were generated by adding grounded ice to the ICE–5G v 1.3 topography within specified latitudinal ranges and for $H < 700$ m, with no isostatic

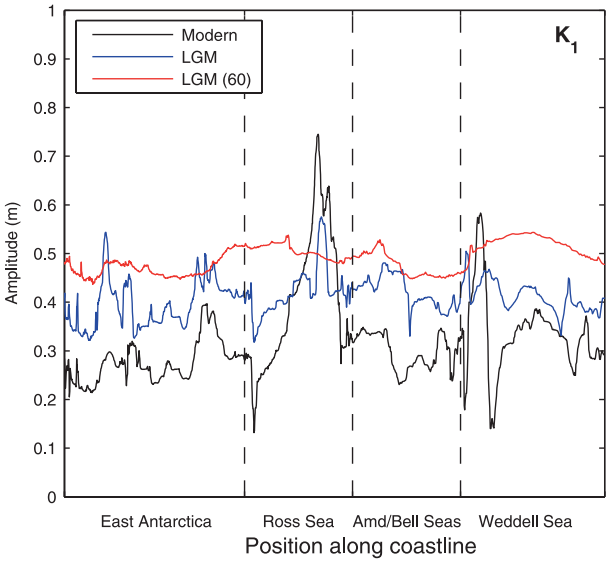

FIG. 7. The K_1 tidal amplitude around the Antarctic coastline, modeled with $M = 720$. Each line gives the amplitude for a different ice margin with the colors corresponding to the configurations shown in Fig. 8.

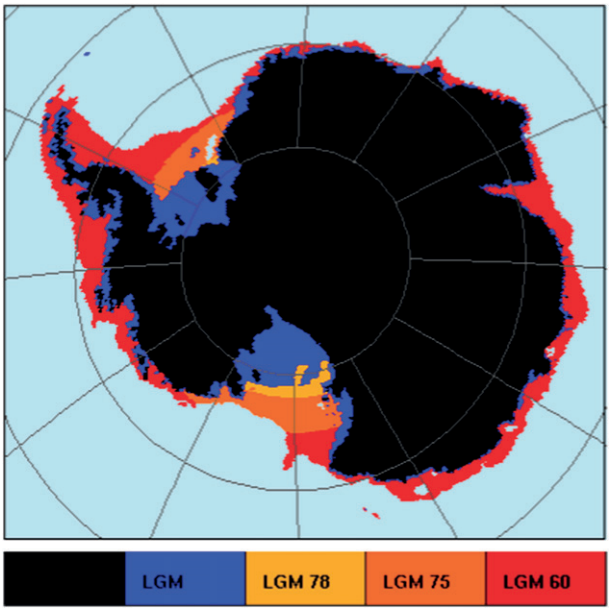

FIG. 8. Antarctic ice margins. Shown are the present-day model (black), the standard LGM model from ICE-5G v 1.3, and three models with extended ice margins.

adjustment. The most extreme configuration, denoted LGM 60 and with grounded ice poleward of 60°S wherever $H < 700$ m, resembles the maximum extent of grounded ice for which there is geological evidence (Anderson et al. 2002, their Fig. 13).

In this configuration the coastline is now rather smooth, with only the Antarctic Peninsula acting as a weak barrier to the Kelvin waves. As shown in Figs. 6g–i and 7, the K_1 tidal amplitude is then quite uniform around the coastline, taking a value of about 50 cm. This represents a significant increase over the average amplitude of approximately 30 cm for the present-day configuration.

b. The M_2 tide

In principle, the same ideas of Kelvin wave propagation around the Antarctic coastline also apply to semidiurnal tides. Taking $H = 2000$ m and $\theta_0 = 70°$ as before, (10) implies $\omega_2 = 1.3 \times 10^{-4}\,\mathrm{s}^{-1}$ and $\omega_3 = 1.9 \times 10^{-4}\,\mathrm{s}^{-1}$, bounding the semidiurnal frequency. This is consistent with the results of Platzman et al. (1981), who reported Antarctic normal modes with zonal wavenumbers 2 and 3, and with periods of 15 and 10 h, respectively.

Shown in Fig. 9 are M_2 solutions for the present-day, LGM, and the extended ice LGM 60 scenario. In all cases, the M_2 tide certainly has a strong signature of zonal wavenumbers 2 and 3, but unlike the K_1 tide, these do not take the simple form of propagating Kelvin waves. At these zonal wavelengths, the tide has the same scale as many of the coastal irregularities, such as the Weddell Sea. Kelvin waves of M_2 frequency are therefore unable to propagate past such features without considerable interaction. The picture is further complicated by strong interactions with remote tides, including those of Patagonia and New Zealand. The latter are clear in the enhanced tidal amplitudes at about 170°W, extending all the way to 50°S.

A more detailed view of the present-day coastal tidal amplitude is shown in Fig. 10. There are two small regions of highly localized tides: one under the Amery ice shelf and another at the southern edge of the Ross Sea. The entire Weddell Sea also has amplified tides, taking the form of short wavelength Kelvin waves (Figs. 9b,c). The tidal amplitude there (shown in Fig. 9a) has the classic form for a rectangular gulf, originally calculated by Taylor (1921) and reproduced in Gill (1982).

In the standard LGM configuration, the M_2 tide is amplified to over 4 m in both the Ross Sea and Weddell Sea. These amplifications appear to occur due to independent local resonances of the partially ice-filled seas. These local resonances lead to amplified tides along the rest of the coastline, where tidal amplitudes approach 1 m (Fig. 10). The amplification in the Ross Sea is highly sensitive to the coastal bathymetry, and even a small outward shift of the grounding line to the LGM 78 configuration (Fig. 8) considerably reduces this tide (Fig. 10). However, the tide in the Weddell Sea is more robust, and the grounding line must be advanced to the

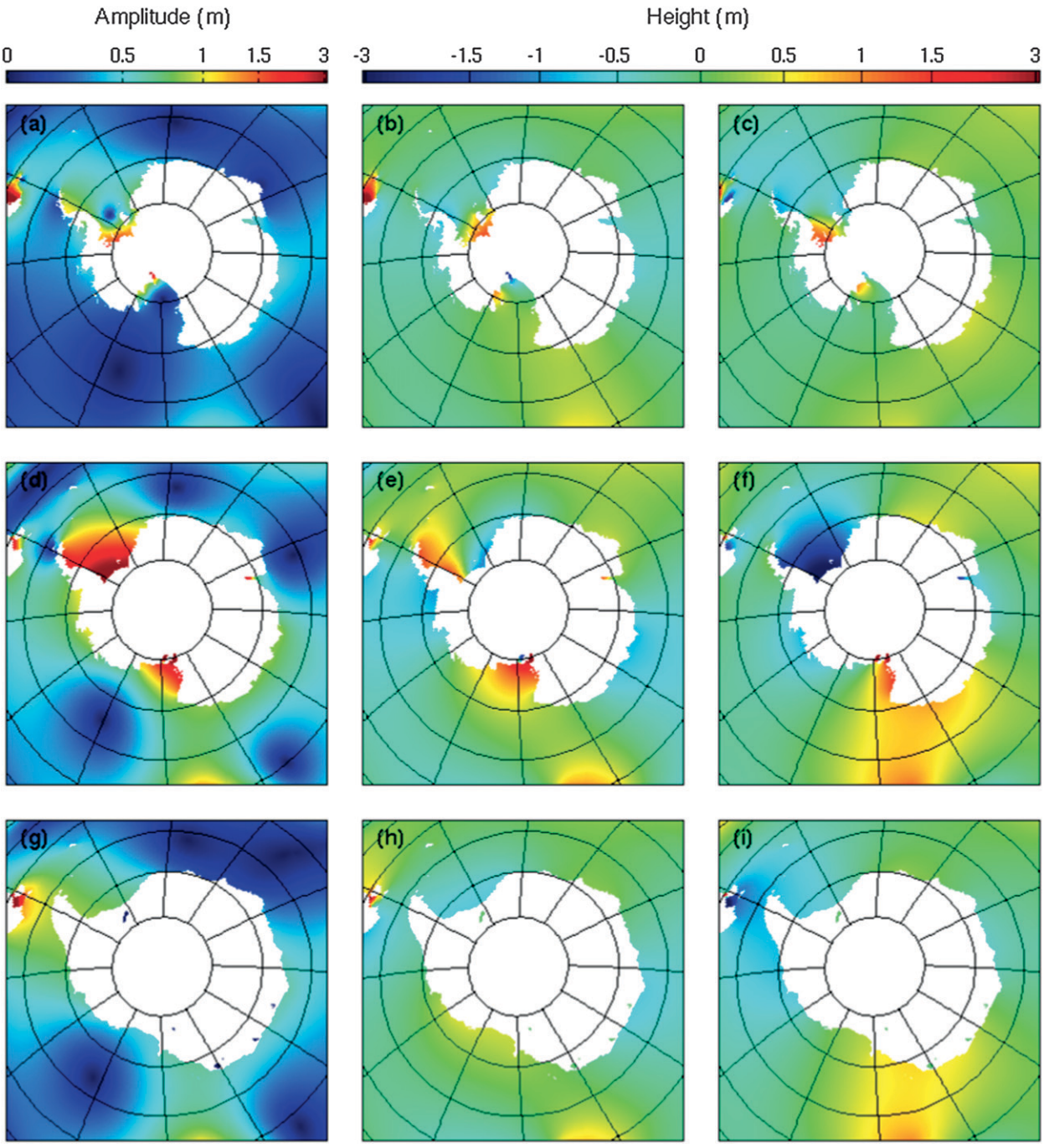

FIG. 9. The M_2 tides (calculated at $M = 720$) for the (top) present-day model, (middle) LGM model, and (bottom) LGM 60 model with grounded ice occupying the entire continental shelf. (middle), (right) Instantaneous snapshots of the tide separated by one-quarter of a tidal period.

LGM 75 configuration for a corresponding reduction. In the extreme LGM 60 configuration, tidal amplitudes fall to less than 1 m along the entire coastline (Fig. 10), with remote interactions appearing to strongly influence the solution (Fig. 9g).

5. Arctic tides

Modeled K_1 tides in the Arctic Ocean are small for both present day and LGM, as shown in Figs. 4b,d,f. Modeled present-day M_2 tides are also small (Figs. 11a–c), although

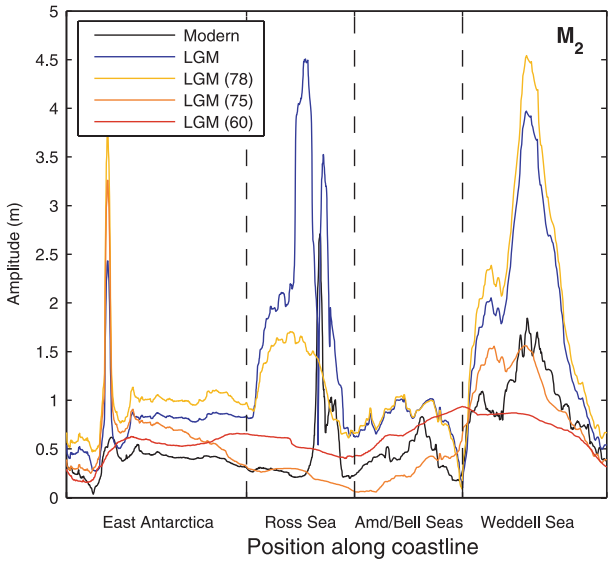

FIG. 10. Modeled M_2 tidal amplitudes (at $M = 720$) around the Antarctic coastline. Each line gives the amplitude for a different ice margin with the colors corresponding to the configurations shown in Fig. 8.

there are larger tides in adjoining seas. These results are consistent with existing models of Arctic tides (e.g., Kowalik and Proshutinsky 1994). In contrast, at LGM the Arctic Ocean has a strong M_2 tide with an approximately annular structure (Fig. 11d). Snapshots of the tide separated by one-quarter of a tidal period (Figs. 11e,f) reveal this tide to be a zonal wavenumber-1 Kelvin wave, propagating cyclonically around the interior of the Arctic Basin. This tide is analagous to the K_1 tide of Antarctica, which propagates anticyclonically around the continental exterior. Indeed, the Arctic tide can be described using the model of section 4a, by replacing the polar continent with a polar basin with depth of the form (8). Now, since the tide must decay poleward (away from the coastline), from (11) the admitted solution of (9) is proportional to $A_+(\theta)$. As expected, this corresponds to an eastward-traveling wave, with the coast on the right (left) in the Northern (Southern) Hemisphere.

As explained in our recent study (Griffiths and Peltier 2008), this tide is made possible at LGM by the disappearance of the Barents Sea, the closure of the Bering Strait, and the elimination of the shallow seas around the Queen Elizabeth Islands, transforming the Arctic Ocean to a basinlike configuration. This alone does not guarantee a large-amplitude tide. However, the LGM Arctic Basin is near to resonance at semidiurnal frequencies: using (10) with $H_0 = 3000$ m and $\theta_0 = 80°$ implies $\omega_1 = 1.5 \times 10^{-4}$ s^{-1}. Explicit calculation of normal modes of the LGM Arctic Ocean confirms that the zonal wavenumber-1 Kelvin wave is indeed close to resonance (Griffiths and Peltier 2008). Note that since the other Kelvin wave normal modes occur at higher frequencies $\omega_2, \omega_3, \ldots$, the K_1 tide cannot be near resonant in the same way.

As in Antarctica, the M_2 tide is sensitive to the assumed shape of the ice margins. In the ICE-5G v. 1.3 reconstruction used thus far, the Innuitian ice sheet entirely covers the present-day Queen Elizabeth Islands (QEI), which lie between 75°–80°N and 90°–120°W. However, there is some doubt as to the exact position of the grounding line of this ice sheet at LGM, and at times some or all of the shallow water surrounding the present-day QEI would have been exposed (Dyke et al. 2002; England et al. 2006). Indeed, this is the configuration of the ICE-5G v 1.2 reconstruction, used in our previous study (Griffiths and Peltier 2008). The modeled M_2 tides for this topographic reconstruction are shown in Figs. 11g–i. The character of a zonal wavenumber-1 Kelvin wave is still evident, but there is a second feature that is massively amplified around the QEI, with tides in excess of 8 m (Fig. 12), as shown in Griffiths and Peltier (2008).

We now examine the sensitivity of these Arctic tides in more detail, by considering configurations where the grounding line of the Innuitian ice sheet is taken to lie between the extremes of Figs. 11d,g. These configurations were generated by adding grounded ice to the ICE-5G v 1.2 topography between 90° and 120°W and for $H < 700$ m, with no isostatic adjustment. The grounding line was taken at either 76°, 77°, 78°, or 79°N, corresponding to a northward advance of approximately 100 km in each case. The coastal amplitudes of the modeled tides are shown in Fig. 12. Note how the amplitude of the tides around the QEI initially increases (to over 11 m) as the grounding line moves northward, but decreases dramatically when taken beyond 77°N. In the final configuration, with grounded ice to 79°N, the tide has an approximately annular structure, with an amplitude of about 1 m for much of the Arctic coastline. This is similar to the tide shown in Fig. 11d, obtained using the ICE-5G v 1.3 topography.

6. Discussion

Our results suggest that polar tides would have been considerably larger at LGM than during the present day. These changes are mainly driven by the sea level drop of about 120 m and the advance of ice sheets onto the continental shelves, leading to quite different coastal configurations at the poles (e.g., Figs. 8 and 11). In our standard model, using the new ICE-5G v 1.3 topographic reconstruction, Antarctic semidiurnal tides are

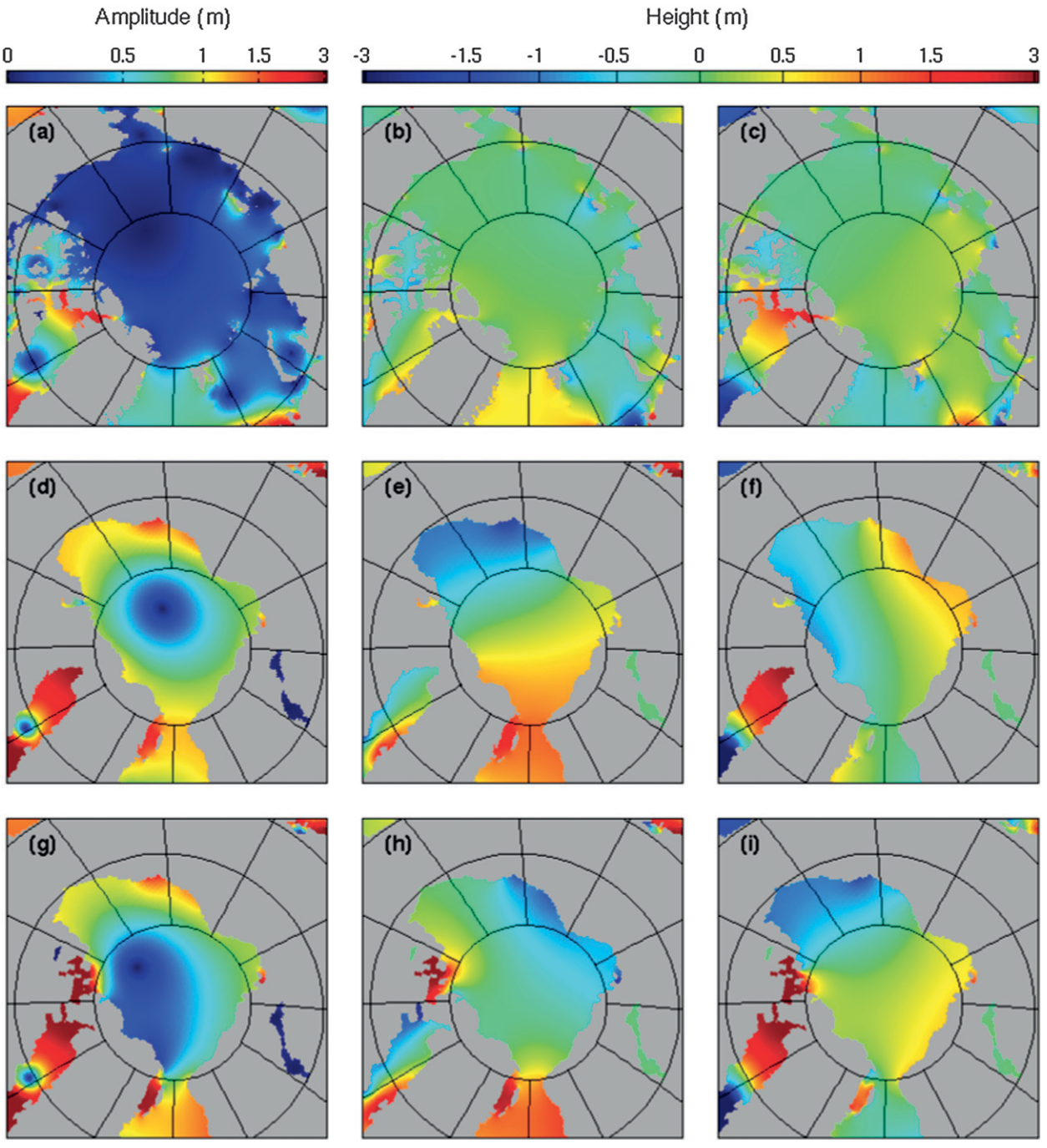

FIG. 11. The M_2 tides (calculated at $M = 720$) for the (top) present-day model, (middle) standard LGM model using ICE-5G v 1.3, and (bottom) LGM model using ICE-5G v 1.2. (middle), (right) Instantaneous snapshots of the tide separated by one-quarter of a tidal period.

amplified to more than 4 m in the Ross and Weddell Seas due to a near-resonance when the continental shelf is approximately half occupied with grounded ice. Both Antarctic diurnal tides and Arctic semidiurnal tides are amplified by a similar Kelvin wave resonance, which is strong because of the effective length of the coastline and coherent because the coastlines are relatively smooth during glacial conditions. This leads to amplified tides around the entire coastline, in excess of 50 cm for Antarctica and 1 m for the Arctic.

All of these amplitudes are sensitive to the assumed margins of the grounded polar ice sheets, the locations

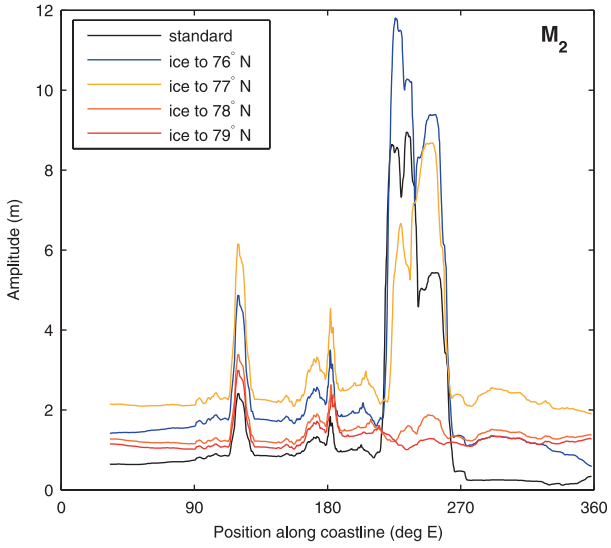

FIG. 12. Modeled M_2 tidal amplitude (at $M = 720$) around the Arctic coastline, for simulations based on the ICE-5G v 1.2 bathymetry. The longitudes given are approximate, because the coastline winds back on itself in several places. The line color indicates the extent of grounded ice around the Queen Elizabeth Islands.

of which would have been changing continuously (e.g., Tarasov and Peltier 2004), and whose precise extent at any given time is not well known. We have illustrated how even small shifts of the grounding lines can lead to large changes in tidal amplitudes at both poles (Figs. 7, 10, and 12). When the Innuitian ice sheet is appropriately extended, our analysis predicts megatides with amplitudes of about 10 m in the Canadian Archipelago, consistent with our previous study (Griffiths and Peltier 2008). Because of great uncertainty in the extent of fringing ice shelves, we have not considered their possible impact. However, the implied reduction in water depth would alter wave propagation characteristics and impact tidal amplitudes to some degree.

The precise amplitude of these modeled tides must be treated with some caution. First, there are uncertainties in our assumptions about the LGM ocean, relating to the depth and coastal configuration, and the model-derived stratification (required for the internal tide drag scheme). Second, there are uncertainties associated with our modeling approach. For instance, nonlinear momentum advection (presently neglected) may play a moderating role where large amplitude tides are highly localized, while interactions between tidal constituents are neglected and the form of the prescribed internal tide drag is approximate. Finally, as discussed in section 3a, there are uncertainties associated with an overestimate of tidal amplitudes at finite model resolution. Although this can be remedied by artificially enhancing the internal tide drag, we rather anticipate a 10%–20% reduction in modeled tidal amplitudes as the resolution increases. Since the spatial pattern of the modeled tides is not resolution dependent, this does not influence our main conclusions that polar tides were (i) amplified at LGM and (ii) highly sensitive to the location of ice sheet grounding lines. Such behavior is expected not only at LGM, but also during other glacial periods of the Late Pleistocene.

Tides and polar climate

Tides impact polar climate in a variety of ways. The generation of internal waves, which can break locally leading to vertical mixing, modifies the temperature and salinity of the water column. Sea ice distribution is influenced by such temperature changes, and by direct fracturing and movement by horizontal tidal currents. Accounting for both of these processes, Holloway and Proshutinsky (2007) demonstrated a role for tides in the sea ice and heat budgets of the Arctic Ocean. Robertson et al. (1998) concluded that tidal currents and mixing strongly influence the circulation and heat flux in the Weddell Sea, and thus the formation of Antarctic Bottom Water, which in turn is coupled to the global ocean circulation. Our results suggest that large polar tides under glacial conditions would have led to greater vertical mixing of the water column than at present, impacting such processes. Since the strongest mixing would occur equatorward of 74° [see the comments leading to (5)], this conclusion does not apply in the high Arctic, or in the Ross and Weddell Seas.

Tides also influence grounded marine ice streams and floating ice shelves. Buckling and crevassing of ice shelves by vertical tidal motions causes them to weaken, perhaps directly leading to their collapse, or preconditions them for other destabilization mechanisms (e.g., Hulbe et al. 2004). The flow of ice sheets is modified by tidal processes close to the grounding line, with the effects being felt far inland, as recorded in present-day Antarctica (e.g., Bindschadler et al. 2003; Gudmundsson 2006). Such effects would have been stronger during glacial times, because of the greater extent of fringing ice and the larger tidal amplitudes predicted by our analysis.

Given the sensitivity of tides to the extent of marine ice streams (and shelves), there is the possibility of an interesting coupling between ice stream extent and tides. For instance, consider the advance of an ice stream onto a continental shelf, in a location where this causes tidal amplitudes to increase at the grounding line. (This would occur between Figs. 9a,d, for semidiurnal tides in the Ross and Weddell Seas.) Eventually, tidal amplitudes could become large enough to cause

the breakup of a connected ice shelf, or to lead to enhanced calving at the grounding line. This might result in a steady state, with the tide effectively determining the ice shelf extent or grounding line location.

Alternatively, the large-amplitude tides might completely destabilize the marine ice sheet, leading to a coastward retreat of the grounding line and the discharge of ice into the ocean. Although the mechanism for such a tidally induced instability remains unknown, such a scenario is possible given the sensitivity of ice streams to sea level at the grounding line (e.g., Schoof 2007). This could naturally lead to a cyclical behavior of ice stream advance onto the continental shelf followed by a tidally induced collapse, with the time scale between events being simply that for the regeneration of a sufficiently large marine ice sheet.

Such behavior is reminiscent of the episodic periods of instability suffered by the Laurentide ice sheet during the late Pleistocene, known as Heinrich events (e.g., Hemming 2004). These events, during which large volumes of ice were discharged into the North Atlantic from close to the mouth of the present-day Hudson Strait, are associated with rapid climate change. The much smaller Innuitian ice sheet appears to have suffered a similar episodic instability, leading to ice discharge into the Arctic Ocean from the Queen Elizabeth Islands (Darby et al. 2002). In this scenario, the large-amplitude tides of the Labrador Sea are implicated in the collapse of the Laurentide ice sheet (Arbic et al. 2004b, 2008), while the megatides around the Queen Elizabeth Islands are implicated in the collapse of the Innuitian ice sheet (Griffiths and Peltier 2008).

Under glacial conditions, our tidal model predicts large tides around the Antarctic coastline, with particular amplifications in the Ross and Weddell Seas. If tides are implicated in the Northern Hemisphere instability events, it is therefore natural to ask whether the large marine ice sheets of Antarctica suffered similar episodic events of catastrophic instability. Unfortunately, data from around Antarctica and the Southern Ocean is much more sparse than that from the North Atlantic, so that relatively little can be inferred about Antarctic ice sheet stability. Although there is evidence of ice discharge events (e.g., Kanfoush et al. 2002) reaching as far away as New Zealand (Carter et al. 2002), it is not clear that these are a southern analog of Heinrich events (Ó Cofaigh et al. 2001). Nevertheless, Kanfoush et al. (2000) argued for the occurrence of episodic instability of grounded ice sheets in the Weddell Sea, with a similar time scale (of about 10 000 yr) to Heinrich events. Our analysis predicts large tides (with amplitudes in excess of 3 m) in the Weddell Sea under glacial conditions (Figs. 9d and 10).

An important aspect of these ice-discharge events is their apparent entrainment to particular phases of the Dansgaard–Oeschger oscillation (e.g., Sakai and Peltier 1998). Heinrich events were apparently entrained to cold phases (e.g., Hemming 2004), while Kanfoush et al. (2000) suggested that the Antarctic ice-discharge events were entrained to warm phases. Note that a period of relative warmth or cold could lead to a small migration of the grounding line, which, as shown here, could lead to a significant change in tidal amplitude for a sufficiently large ice sheet. Thus, a tidally induced destabilization mechanism would be sensitive to climate conditions and is thus consistent with the timing of past ice-discharge events.

Acknowledgments. This paper is a contribution to the work of the Polar Climate Stability Network, which is funded by the Canadian Foundation for Climate and Atmospheric Science, and by a consortium of Canadian universities. Additional support has been provided from NSERC Discovery Grant A9627. Thanks to Guido Vettoretti for preparing the CSM 1.4 dataset for our use and to Rosemarie Drummond for preparing the ICE-5G v 1.3 bathymetry.

REFERENCES

Adkins, J. F., K. McIntyre, and D. P. Schrag, 2002: The salinity, temperature, and δ^{18}O of the glacial deep ocean. *Science,* **298,** 1769–1773.

Anderson, J. B., S. S. Shipp, A. L. Lowe, J. S. Wellner, and A. B. Mosola, 2002: The Antarctic ice sheet during the Last Glacial Maximum and its subsequent retreat history: A review. *Quat. Sci. Rev.,* **21,** 49–70.

Antonov, J. I., R. A. Locarnini, T. P. Boyer, A. V. M. Mishonov, and H. E. Garcia, 2006: *Salinity*. Vol. 2, *World Ocean Atlas 2005,* NOAA Atlas NESDIS 62, 182 pp.

Arbic, B. K., S. T. Garner, R. W. Hallberg, and H. L. Simmons, 2004a: The accuracy of surface elevations in forward global barotropic and baroclinic tide models. *Deep-Sea Res.,* **51,** 3069–3101.

——, D. R. MacAyeal, J. X. Mitrovica, and G. A. Milne, 2004b: Palaeoclimate: Ocean tides and Heinrich events. *Nature,* **432,** 460, doi:10.1038/432460a.

——, P. St-Laurent, G. Sutherland, and C. Garrett, 2007: On the resonance and influence of the tides in Ungava Bay and Hudson Strait. *Geophys. Res. Lett.,* **34,** L17606, doi:10.1029/2007GL030845.

——, J. X. Mitrovica, D. R. MacAyeal, and G. A. Milne, 2008: On the factors behind large Labrador Sea tides during the last glacial cycle and the potential implications for Heinrich events. *Paleoceanography,* **23,** PA3211, doi:10.1029/2007PA001573.

Bindschadler, R. A., M. A. King, R. B. Alley, S. Anandakrishnan, and L. Padman, 2003: Tidally controlled stick-slip discharge of a West Antarctic ice stream. *Science,* **301,** 1087–1089, doi:10.1126/science.1087231.

Carrère, L., and F. Lyard, 2003: Modeling the barotropic response of the global ocean to atmospheric wind and pressure

forcing—Comparisons with observations. *Geophys. Res. Lett.,* **30,** 1275, doi:10.1029/2002GL016473.

Carter, L., H. L. Neil, and L. Northcote, 2002: Late Quaternary ice-rafting events in the SW Pacific Ocean, off eastern New Zealand. *Mar. Geol.,* **191,** 19–35.

Darby, D. A., J. F. Bischof, R. F. Spielhagen, S. A. Marshall, and S. W. Herman, 2002: Arctic ice export events and their potential impact on global climate during the late Pleistocene. *Paleoceanography,* **17,** 1025, doi:10.1029/2001PA000639.

Dyke, A. S., J. T. Andrews, P. U. Clark, J. H. England, G. H. Miller, J. Shaw, and J. J. Veillette, 2002: The Laurentide and Innuitian ice sheets during the Last Glacial Maximum. *Quat. Sci. Rev.,* **21,** 9–31.

Egbert, G. D., and R. D. Ray, 2003: Semi-diurnal and diurnal tidal dissipation from TOPEX/Poseidon altimetry. *Geophys. Res. Lett.,* **30,** 1907, doi:10.1029/2003GL017676.

——, A. F. Bennett, and M. G. G. Foreman, 1994: TOPEX/POSEIDON tides estimated using a global inverse model. *J. Geophys. Res.,* **99,** 24 821–24 852.

——, R. D. Ray, and B. G. Bills, 2004: Numerical modeling of the global semidiurnal tide in the present day and in the last glacial maximum. *J. Geophys. Res.,* **109,** C03003, doi:10.1029/2003JC001973.

England, J., N. Atkinson, J. Bednarski, A. S. Dyke, D. A. Hodgson, and C. Ó. Cofaigh, 2006: The Innuitian Ice Sheet: Configuration, dynamics and chronology. *Quat. Sci. Rev.,* **25,** 689–703, doi:10.1016/j.quascirev.2005.08.007.

Farrell, W. E., 1973: Deformation of the earth by surface loads. *Rev. Geophys. Space Phys.,* **10,** 761–797.

Garrett, C., 1972: Tidal resonance in the Bay of Fundy and Gulf of Maine. *Nature,* **238,** 441–443, doi:10.1038/238441a0.

——, and E. Kunze, 2007: Internal tide generation in the deep ocean. *Annu. Rev. Fluid Mech.,* **39,** 57–87, doi:10.1146/annurev.fluid.39.050905.110227.

Gill, A. E., 1982: *Atmosphere–Ocean Dynamics*. Academic Press, 662 pp.

Griffiths, S. D., and R. H. J. Grimshaw, 2007: Internal tide generation at the continental shelf modeled using a modal decomposition: Two-dimensional results. *J. Phys. Oceanogr.,* **37,** 428–451.

——, and W. R. Peltier, 2008: Megatides in the Arctic Ocean under glacial conditions. *Geophys. Res. Lett.,* **35,** L08605, doi:10.1029/2008GL033263.

Gudmundsson, G. H., 2006: Fortnightly variations in the flow velocity of Rutford Ice Stream, West Antarctica. *Nature,* **444,** 1063–1064, doi:10.1038/nature05430.

Hemming, S. R., 2004: Heinrich events: Massive late Pleistocene detritus layers of the North Atlantic and their global climate imprint. *Rev. Geophys.,* **42,** RG1005, doi:10.1029/2003RG000128.

Hendershott, M. C., 1972: The effects of solid earth deformation on global ocean tides. *Geophys. J. Int.,* **29,** 389–402.

Holloway, G., and A. Proshutinsky, 2007: Role of tides in Arctic ocean/ice climate. *J. Geophys. Res.,* **112,** C04S06, doi:10.129/2006JC003643.

Hulbe, C. L., D. R. MacAyeal, G. H. Denton, J. Kleman, and T. V. Lowell, 2004: Catastrophic ice shelf breakup as the source of Heinrich event icebergs. *Paleoceanography,* **19,** PA1004, doi:10.1029/2003PA000890.

Jayne, S. R., and L. C. St. Laurent, 2001: Parameterizing tidal dissipation over rough topography. *Geophys. Res. Lett.,* **28,** 811–814.

Kanfoush, S. L., D. A. Hodell, C. D. Charles, T. P. Guilderson, P. G. Mortyn, and U. S. Ninnemann, 2000: Millennial-scale instability of the Antarctic ice sheet during the last glaciation. *Science,* **288,** 1815–1818.

——, ——,——, T. R. Janecek, and F. R. Rack, 2002: Comparison of ice-rafted debris and physical properties in ODP Site 1094 (South Atlantic) with the Vostok ice core over the last four climatic cycles. *Palaeogeogr. Palaeoclimatol. Palaeoecol.,* **182,** 329–349.

Kowalik, Z., and A. Y. Proshutinsky, 1994: The Arctic Ocean tides. *The Polar Oceans and Their Role in Shaping the Global Environment, Geophys. Monogr.,* Vol. 85, Amer. Geophys. Union, 137–158.

Locarnini, R. A., A. V. Mishonov, J. I. Antonov, T. P. Boyer, and H. E. Garcia, 2006: *Temperature*. Vol. 1, *World Ocean Atlas 2005,* NOAA Atlas NESDIS 61, 182 pp.

Lyard, F., F. Lefevre, T. Letellier, and O. Francis, 2006: Modelling the global ocean tides: Modern insights from FES2004. *Ocean Dyn.,* **56,** 394–415, doi:10.1007/s10236-006-0086-x.

Montenegro, Á., M. Eby, A. J. Weaver, and S. R. Jayne, 2007: Response of a climate model to tidal mixing parameterization under present day and Last Glacial Maximum conditions. *Ocean Modell.,* **19,** 125–137, doi:10.1016/j.ocemod.2007.06.009.

Munk, W., and B. Bills, 2007: Tides and the climate: Some speculations. *J. Phys. Oceanogr.,* **37,** 135–147.

Ó Cofaigh, C., J. A. Dowdeswell, and C. J. Pudsey, 2001: Late Quaternary iceberg rafting along the Antarctic Peninsula continental rise and in the Weddell and Scotia seas. *Quat. Res.,* **56,** 308–321, doi:10.1006/qres.2001.2267.

Peltier, W. R., 1996: Mantle viscosity and ice-age ice sheet topography. *Science,* **273,** 1359–1364, doi:10.1126/science.273.5280.1359.

——, 1998: Postglacial variations in the level of the sea: Implications for climate dynamics and solid-earth geophysics. *Rev. Geophys.,* **36,** 603–689.

——, 2004: Global glacial isostasy and the surface of the ice-age earth: The ICE-5G (VM2) Model and GRACE. *Annu. Rev. Earth Planet. Sci.,* **32,** 111–149, doi:10.1146/annurev.earth.32.082503.144359.

——, and L. P. Solheim, 2004: The climate of the earth at Last Glacial Maximum. Statistical equilibrium state and a mode of internal variability. *Quat. Sci. Rev.,* **23,** 335–357, doi:10.1016/j.quascirev.2003.07.003.

——, and R. G. Fairbanks, 2006: Global glacial ice volume and Last Glacial Maximum duration from an extended Barbados sea level record. *Quat. Sci. Rev.,* **25,** 3322–3337, doi:10.1016/j.quascirev.2006.04.010.

Platzman, G. W., 1984: Normal modes of the World Ocean. Part IV: Synthesis of diurnal and semidiurnal tides. *J. Phys. Oceanogr.,* **14,** 1532–1550.

——, G. A. Curtis, K. S. Hansen, and R. D. Slater, 1981: Normal modes of the World Ocean. Part II: Description of modes in the period range 8 to 80 hours. *J. Phys. Oceanogr.,* **11,** 579–603.

Robertson, R., L. Padman, and G. D. Egbert, 1998: Tides in the Weddell Sea. *Ocean, Ice, and Atmosphere: Interactions at the Antarctic Continental Margin,* S. S. Jacobs and R. F. Weiss, Eds., Antarctic Research Series, Vol. 75, Amer. Geophys. Union, 341–359.

Sakai, K., and W. R. Peltier, 1998: Deglaciation-induced climate variability: An explicit model of the glacial-interglacial transition that simulates both the Bolling/Allerod and Younger-Dryas events. *J. Meteor. Soc. Japan,* **76,** 1029–1044.

Schoof, C., 2007: Ice sheet grounding line dynamics: Steady states, stability, and hysteresis. *J. Geophys. Res.,* **112,** F03S28, doi:10.1029/2006JF000664.

Shennan, I., and B. Horton, 2002: Holocene land- and sea-level changes in Great Britain. *J. Quat. Sci.,* **17,** 511–526, doi:10.1002/jqs.710.

Simmons, H. L., R. W. Hallberg, and B. K. Arbic, 2004: Internal wave generation in a global baroclinic tide model. *Deep-Sea Res.,* **51,** 3043–3068.

Tarasov, L., and W. R. Peltier, 2004: A geophysically constrained large ensemble analysis of the deglacial history of the North American ice-sheet complex. *Quat. Sci. Rev.,* **23,** 359–388, doi:10.1016/j.quascirev.2003.08.004.

Taylor, G. I., 1920: Tidal friction in the Irish Sea. *Phil. Trans. Roy. Soc. London,* **220,** 1–33.

——, 1921: Tidal oscillations in gulfs and rectangular basins. *Proc. London Math. Soc.,* **20,** 148–181.

Thomas, M., and J. Sündermann, 1999: Tides and tidal torques of the world ocean since the last glacial maximum. *J. Geophys. Res.,* **104,** 3159–3183.

Uehara, K., 2005: Changes of ocean tides along Asian coasts caused by the post glacial sea-level change. *Mega-Deltas of Asia: Geological Evolution and Human Impact,* Z. Chen, Y. Saito, and S. L. Goodbred Jr., Eds., China Ocean Press, 227–232.

——, J. D. Scourse, K. J. Horsburgh, K. Lambeck, and A. P. Purcell, 2006: Tidal evolution of the northwest European shelf seas from the Last Glacial Maximum to the present. *J. Geophys. Res.,* **111,** C09025, doi:10.1029/2006JC003531.

Williams, G., 2000: Geological constraints on the Precambrian history of Earth's rotation and the Moon's orbit. *Rev. Geophys.,* **38,** 37–59.

Wunsch, C., 2000: Moon, tides and climate. *Nature,* **405,** 743–744.

——, 2005: Speculations on a schematic theory of the Younger Dryas. *J. Mar. Res.,* **63,** 315–333.